Anisotropic X-Ray Dark-Field Tomography: A Continuous Model and its Discretization

M. Wieczorek,[1,*] F. Schaff,[2] F. Pfeiffer,[2,3] and T. Lasser[1]
[1]Computer Aided Medical Procedures, Technische Universität München, 85748 Garching, Germany
[2]Lehrstuhl für Biomedizinische Physik, Physik-Department and Institut für Medizintechnik, Technische Universität München, 85748 Garching, Germany
[3]Institut für diagnostische und interventionelle Radiologie, Klinikum rechts der Isar, Technische Universität München, 81675 München, Germany

(Received 7 June 2016; published 5 October 2016)

The x-ray dark-field signal measured in grating interferometers is anisotropic, depending on both the beam direction and the grating orientation with respect to the sample. We present a novel general closed-form, continuous forward model of the anisotropic dark-field signal. Furthermore, we derive a discretization using spherical harmonics, leading to a large-scale linear inverse problem. We present first experimental results of a wooden sample, demonstrating marked advantages over previous results, in particular, the resolution of multiple scattering directions in one volume element.

DOI: 10.1103/PhysRevLett.117.158101

Introduction.—Modern grating-based x-ray imaging enables the extraction of phase-contrast (refraction) and dark-field (scattering) information in addition to the conventional measurement of absorption [1–4]. The dark-field signal provides scattering information at the subpixel level and has shown great utility in several fields of application. Among others, there have been promising studies regarding breast imaging [5,6], lung imaging [7,8], microbubbles as contrast agents [9], and musculoskeletal imaging [10,11] as well as materials testing [12].

Contrary to conventional absorption or phase-contrast data, the dark-field signal is orientation dependent; i.e., the measured signal depends on both the orientation of the imaged sample and the orientation of the x rays. As a grating interferometry setup is sensitive only to signals orthogonal to the grating bars, the anisotropic scattering signal can be measured and recorded [13].

In order to perform a tomographic reconstruction of this anisotropic signal, Malecki *et al.* derived a model of coherent superposition for directional dark-field imaging [14]. This led to a forward model based on the discrete superposition, enabling component-based tomographic reconstructions of the anisotropic signal. After the reconstruction of the components, rank-2 tensors were fitted for each volume element [15]. The method is called x-ray tensor tomography (XTT) and recovers the covariance of the scattering assuming a Gaussian scattering model [13]. Vogel *et al.* [16] then showed that XTT can be formulated as a regular linear inverse problem, allowing the application of established iterative reconstruction methods. The XTT method is outlined schematically in Fig. 1. XTT has shown the capability of resolving directional information within carbon fiber samples [15], dentinal tubules, and wooden samples [16]. Recently, Jud *et al.* [17] studied structural information recovered from both microCT and XTT. They concluded that XTT can successfully extract dentinal tubules (~2 μm) using a significantly lower-resolution imaging setup than microCT. In contrast to XTT, the sample had to be irreversibly cut for microCT such that it fit the field of view, in order to achieve the high resolution necessary for the extraction of the dentinal tubules.

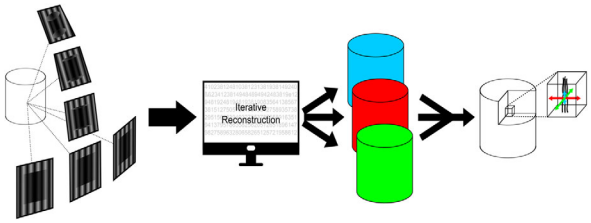

FIG. 1. Schematic overview of XTT: The sample is measured with a grating interferometer from many different orientations sampling the unit sphere. The resulting dark-field images are fed to an iterative reconstruction algorithm. Several component volumes are reconstructed simultaneously, each representing scattering information in a certain direction. Finally, these volumes are merged into tensors and the resulting voxelwise anisotropic scattering information can be used to extract information about subvoxel-sized structures, such as their orientation.

In more detail, the forward model used for XTT is given as follows [14,16].

Definition 1: XTT forward model.—Let L_j denote the path of the x ray corresponding to the jth dark-field measurement $d_j \in \mathbb{R}$. Further let $l_j \in \mathbb{S}_2$ [18] denote the direction of L_j, and $t_j \in \mathbb{S}_2$ the direction orthogonal to the grating bars within the plane defined by the gratings. Choosing a finite set of K scattering directions $u_k \in \mathbb{S}_2$, the squared scattering magnitudes $\eta_k : \mathbb{R}^3 \to \mathbb{R}$ corresponding to u_k at each sample location relate to the dark-field measurement d_j as follows:

$$d_j = \exp\left(-\sum_{k=1}^{K}(|l_j \times u_k|\langle u_k, t_j\rangle)^2 \int_{L_j} \eta_k(x)dx\right). \quad (1)$$

The reconstruction process of XTT thus involves the selection of a finite set of scattering directions u_k, the inversion of the forward model (1) to recover the corresponding scattering magnitudes η_k from the dark-field measurements d_j, and the subsequent fitting of a rank-2 tensor to the scattering data (η_k, u_k) at each volume element (voxel).

While XTT shows very promising results, in particular, for the extraction of the orientation of microstructures (which corresponds to the direction of least scattering in each tensor), there are two major limitations of this method. First, as the dark-field signal corresponds to microstructures which are much smaller than the resolution of the detector, the assumption of a single structure orientation in a single voxel is very restrictive and erroneous as soon as multiple orientations are present at the subvoxel level. In addition, the discrete nature of the forward model (1) limits the possibility of analyzing the measurement process mathematically or to incorporate more natural representations of scattering functions, such as spherical harmonics. Second, the reconstruction results of XTT are not invariant to the selection of the scattering directions u_k. This results in local variations of the reconstructed magnitude, if some parts of the unit sphere are sampled more densely by the u_k than others, and global variations depending on the chosen total number of u_k.

In the following, we present a novel general closed-form, analytical forward model for anisotropic x-ray dark-field tomography (AXDT) using generic spherical functions to represent the scattering magnitudes. This model is independent of the weighting term corresponding to the imaging physics and, thus, easy to adapt to different physical terms. Furthermore, by using generic spherical functions, we eliminate the limitations of rank-2 tensors. In addition, we show that the previous model by Malecki *et al.* [14] is a special case of this continuous model, which subsumes all previous findings, including simulation results, under this new hood. Finally, we provide a concrete reconstruction formula using spherical harmonics to represent the scattering functions, and we show first experimental results demonstrating the capability of resolving multiple scattering directions within single volume elements.

The following two assumptions are made in this work: First, we neglect any effects of polychromaticity and consider only the integrated scattering signal over the entire x-ray spectrum. This is equivalent to what is usually done for attenuation-based computed tomography. Second, we assume an exponential model, as Strobl *et al.* [19] found that the situation of dark-field imaging is equivalent to spin-echo small-angle neutron scattering (SESANS), for which Andersson *et al.* [20] showed that the exponential model accounts for multiscattering.

Methods.—The XTT forward model (1) involves discrete summation over scattering magnitudes weighted according to the corresponding scattering direction. The most natural continuous equivalent of a summation over scaled unit vectors is a surface integral over the unit sphere. For generality, we also replace the concrete weighting of (1) by an abstract weighting function h. This leads to our proposed closed-form continuous model for AXDT.

A continuous forward model: *Definition 2: AXDT continuous forward model.*—Let L_j denote the path of the x ray corresponding to the jth dark-field measurement $d_j \in \mathbb{R}$. Further let $l_j \in \mathbb{S}_2$ denote the direction of L_j and $t_j \in \mathbb{S}_2$ the direction orthogonal to the grating bars within the plane defined by the gratings. The continuous forward model relating the spherical scattering magnitudes $\eta\colon \mathbb{S}_2 \times \mathbb{R}^3 \to \mathbb{R}$ to the dark-field measurement d_j is defined as

$$d_j = \exp\left(-\int_{L_j}\int_{\mathbb{S}_2} h(u, t_j, l_j)\eta(u, x)\frac{d\Omega(u)}{4\pi}dx\right), \quad (2)$$

where $h\colon \mathbb{S}_2 \times \mathbb{S}_2 \times \mathbb{S}_2 \to \mathbb{R}$ denotes a square integrable weighting function and $d\Omega$ denotes the standard solid angle [21].

In the following, we will focus on the discretization of the inner surface integral for efficient practical implementations of the forward model. The outer integral is a standard line integral, for which discretization methods are well known already from the field of conventional computed tomography; see, for example, [22,23].

There are many methods for numerical computation of surface integrals over the sphere, but they all involve approximating the surface integral via a weighted sum of function evaluations at discrete points on the sphere. For an excellent overview on this topic, we refer to Ref. [24]. If one applies a cubature method, for example, using spherical designs [25] using equal weights for all sampling directions, the discrete XTT forward model (1) becomes a special case of the continuous AXDT forward model (2) up to a constant factor depending on the number of evaluation points. In the following, we present the use of spherical harmonics for discretization of the AXDT forward model (2).

Discretization using spherical harmonics: One of the most powerful tools to deal with spherical functions is the set of real-valued spherical harmonics $\{V_k^m\}_{k=0,\ldots,\infty;m=-k,\ldots,k}$. Spherical harmonics provide an orthonormal basis for square integrable functions $f \in \mathcal{L}^2(\mathbb{S}_2)$ [26]; thus, f can be decomposed as

$$f = \sum_{k=0}^{\infty}\sum_{m=-k}^{k} f_k^m V_k^m, \quad (3)$$

where the f_k^m denote the spherical-harmonics coefficients. The index k is commonly called degree and m the order of the respective basis function. For a general overview on spherical harmonics we refer to Ref. [27].

Theorem 1: Spherical-harmonics-based discretization.—Let $\{h_k^m(t_j, l_j)\}$ and $\{\eta_k^m(x)\}$ denote the spherical-harmonics coefficients of $h(\cdot, t_j, l_j)$ and $\eta(\cdot, x)$,

respectively. Further let $K \in \mathbb{N}$ denote a truncation degree. Then a discrete approximation to Eq. (2) in terms of the spherical-harmonics coefficients of η is given as follows:

$$d_j \approx \exp\left(-\frac{1}{4\pi}\sum_{k=0}^{K}\sum_{m=-k}^{k} h_k^m(t_j,l_j)\int_{L_j}\eta_l^m(x)dx\right). \quad (4)$$

Proof.—Consider the inner integral in Eq. (2). By applying Parseval's theorem for spherical harmonics we have

$$\int_{\mathbb{S}_2} h(u,t_j,l_j)\eta(u,x)\frac{d\Omega(u)}{4\pi} = \frac{1}{4\pi}\sum_{k=0}^{\infty}\sum_{m=-k}^{k} h_k^m(t_j,l_j)\eta_k^m(x) \approx \frac{1}{4\pi}\sum_{k=0}^{K}\sum_{m=-k}^{k} h_k^m(t_j,l_j)\eta_k^m(x). \quad (5)$$

Inserting this approximation into the forward model (2) and using the linearity of the integral to swap integral and sum, Eq. (4) follows directly. ∎

As scattering is a symmetric process, it is a valid assumption that the function $h(u,t_j,l_j)$ is point symmetric in $u \in \mathbb{S}_2$ with respect to the origin, i.e., $h(u,t_j,l_j) = h(-u,t_j,l_j)$. This means that $h_k^m(t_j,l_j) = 0$ for any odd degree k. We can thus limit the computation to even degrees, which intrinsically leads to a symmetric reconstructed function $\eta(u,x)$.

AXDT reconstruction as a linear inverse problem: The discretized forward model using spherical harmonics (4) can be used to formulate the recovery of η from the measurements d_j as a linear inverse problem, as was done in Ref. [16] for the XTT forward model (1).

First, we discretize our volume of interest into I cubic voxels. Then we form the system matrix $P \in \mathbb{R}^{J\times I}$ consisting of the discretized line integrals corresponding to each measurement d_j, where $j = 1,\ldots,J$, and J denotes the total number of measurements (the number of detector pixels times the number of dark-field images). Let further $p = [-\ln(d_j)] \in \mathbb{R}^J$ and $W_k^m = \mathrm{diag}(h_k^m(t_1,l_1),\ldots,h_k^m(t_J,l_J))/(4\pi) \in \mathbb{R}^{J\times J}$. Finally, let $[\eta_k^m] \in \mathbb{R}^I$ denote the discretized spherical-harmonics coefficients representing the scattering magnitude η. Then the AXDT reconstruction problem can be formulated as the linear inverse problem

$$p = \sum_{k=0}^{K}\sum_{m=-k}^{k} W_k^m P \eta_k^m = \begin{pmatrix} W_0^0 P & \cdots & W_K^{-K} P & \cdots & W_K^K P \end{pmatrix} \begin{pmatrix} \eta_0^0 \\ \vdots \\ \eta_K^{-K} \\ \vdots \\ \eta_K^K \end{pmatrix}. \quad (6)$$

Experiments and results.—To evaluate our proposed method, we measured a sample consisting of two wooden sticks (see Fig. 2 for an illustration). A wooden stick contains fiberlike structures in the direction of its growth. Thus, the scattering is assumed to be horn-torus-shaped orthogonally to the direction of growth. In the region where the two crossed sticks touch, we expect a superposition of both of the scattering functions corresponding to each stick.

The sample was measured with a symmetrical x-ray grating interferometer with an intergrating distance of 91 cm. Three gratings were used: two 10 μm period absorption gratings

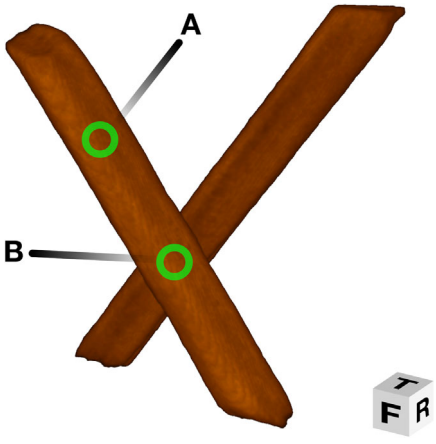

FIG. 2. Volume visualization of the wooden sticks data set. **A** marks a voxel within the front stick (see Fig. 4), while **B** marks a voxel within the region where the two sticks touch (see Fig. 5) (T = top, F = front, and R = right).

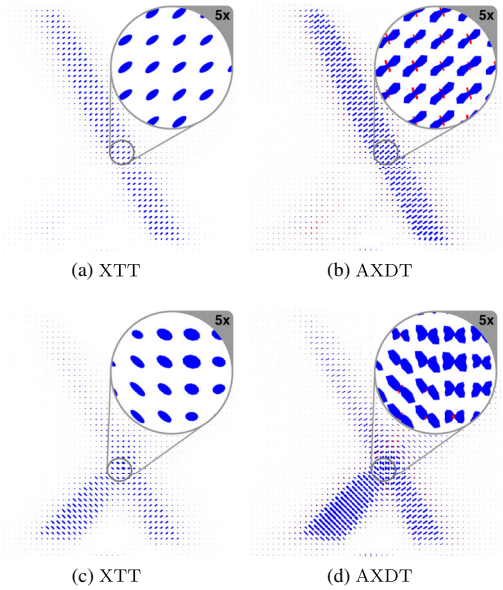

(a) XTT (b) AXDT

(c) XTT (d) AXDT

FIG. 3. Slice visualization of XTT (a,c) and AXDT (b,d) reconstructions. Positive function values are colored blue, while negative ones are displayed in red. The upper row shows the slice parallel to the front plane which contains voxel **A** (see Fig. 2), the bottom row the slice containing voxel **B**. For clarity of visualization, we show only every fifth tensor or scattering function and scale them to comparable sizes.

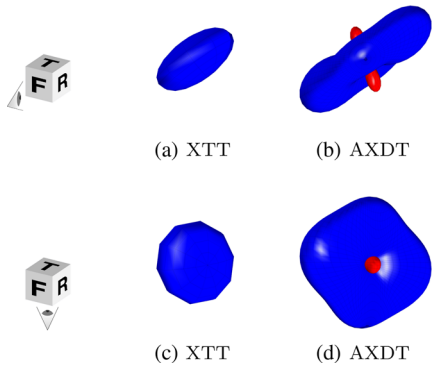

FIG. 4. Scattering function corresponding to voxel **A**, which contains one main structure orientation (see Fig. 2). Positive function values are colored blue, while negative ones are displayed in red. The upper row shows a front view; the bottom row shows a bottom view. From left to right: (a), (c) XTT tensor and (b), (d) AXDT reconstruction.

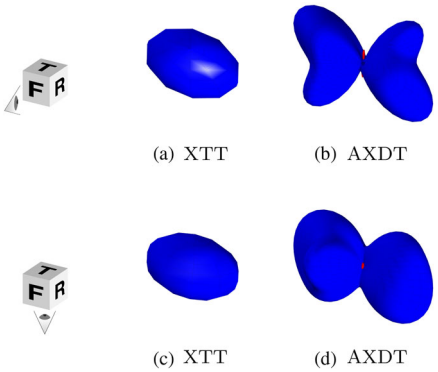

FIG. 5. Scattering function corresponding to voxel **B**, which contains two structure orientations (see Fig. 2). Positive function values are colored blue, while negative ones are displayed in red. The upper row shows a front view; the bottom row shows a bottom view. From left to right: (a), (c) XTT tensor and (b), (d) AXDT reconstruction.

and a 5 μm period phase grating. X rays were generated with a tungsten-target x-ray tube run at 60 kVp and 13.3 mA current. The spectrum was filtered by 2 mm aluminum. A Varian PaxScan 2520D flat-panel detector with a CsI scintillator and 800×800 pixels of size 127 μm^2 was used to record images. For each viewpoint, a series of eight phase-stepping images was acquired with 1 s exposure time each, from which the dark-field images were extracted by first-order Fourier approximation [3]. The recorded raw data were rebinned by a factor of 2 prior to any processing. In total, dark-field images were acquired from 1200 different viewpoints sampling the unit sphere, yielding a total measurement time of 345 min. For details of the setup we refer to Refs. [3,4,28], and Supplemental Material [29].

The reconstruction process was realized in our C++ framework CampRecon [30] for large-scale inverse problems. To compute the system matrix we used a ray-driven multi-GPU projector written in OpenCL developed by Fehringer *et al.* [31]. For the spherical harmonics and the corresponding visualization we used the Matlab toolbox provided by Politis [32]. The entries of the diagonal matrices W_l^m were precomputed. Each reconstruction was computed using 20 iterations of the conjugate gradient method [33]. All computations were performed on a computer equipped with dual Intel Xeon E5-2687W v2 with 128 GB RAM and dual Nvidia GeForce GTX 980Ti GPU accelerators.

For AXDT reconstruction we used the weighting function $h\colon \mathbb{S}_2 \times \mathbb{S}_2 \times \mathbb{S}_2 \to \mathbb{R},\ (u,t,l) \mapsto (|l \times u|\langle u,t\rangle)^2$ from Malecki *et al.* [15]. The linear inverse problem (6) was implemented using $K = 4$ and $m = 0, 2, 4$, exploiting the previously mentioned point symmetries as well as the fact that this particular function h is the product of four functions of spherical-harmonic degree one. The reconstruction process thus effectively computes 15 η_k^m volumes with an isotropic voxel size of 254 μm, and the total time for computations was 50 min.

For comparison we also reconstructed the same data using the previous XTT approach (1) as in Ref. [16] with $N = 13$, effectively computing 13 η_k volumes before performing the rank-2 tensor fit. The total time for computations here was 45 min.

Figure 3 shows slice visualizations of both reconstructions. The two slices were chosen to contain the two voxels **A** and **B** as marked in Fig. 2. Voxel **A** is within the front stick, where the wooden fibers have only one main orientation. The fiber orientation corresponds to the direction of least scattering and is recovered correctly for both the AXDT and XTT reconstructions; see Figs. 3(a) and 3(b). Voxel **B** is in the region where the two sticks touch and accordingly contains two main structure orientations. Here the XTT approach [Fig. 3(c)] fails as expected, while the AXDT approach [Fig. 3(d)] succeeds in distinguishing the two orientations. The scattering functions corresponding to voxels **A** and **B** are shown in detail in Figs. 4 and 5. In particular, Fig. 5 shows the limited usefulness of the rank-2 tensor for multiple structure orientations. It is obvious that the AXDT approach yields reconstructions which contain information that is not retrieved by the XTT approach.

For the AXDT approach, "negative" scattering magnitudes can be observed along the direction of the microstructure of the sample (see Figs. 4 and 5). We currently hypothesize that this is caused by the weighting function h, which does not perfectly describe the measurement if the microstructure is measured along the x-ray direction. Applying a non-negativity constraint in the reconstruction algorithm may solve this issue, along with a better model of weighting.

Because of the similarity of SESANS and dark-field imaging, it may be possible to apply the presented method to SESANS in a similar fashion.

Conclusion.—In this Letter, we presented a novel general closed-form, continuous forward model for anisotropic dark-field imaging, which, to our knowledge, is the first of its kind. This model is independent of the actual

formulation and discretization of the functions h and η and allows mathematical analysis of the anisotropic dark-field imaging process, for example, studying its null space to enable error estimates or simplified acquisition protocols. In addition, we introduced a discretization of the scattering function using real-valued spherical harmonics and derived a large-scale linear inverse problem. This combined new approach, termed AXDT, improves upon the previous XTT approach significantly, leading to scattering magnitudes which are invariant, while allowing the resolution of multiple scattering directions within a single volume element. The latter is of particular interest, as the dark-field signal corresponds to microstructures much below the resolution of the detector. Thus, the presence of multiple microstructure orientations in one single voxel is very likely. A first experiment confirms these findings and demonstrates the future potential of AXDT.

This work was partially funded by the European Research Council (ERC, H2020, AdG 695045), the DFG Cluster of Excellence Munich-Centre for Advanced Photonics (MAP), the DFG Gottfried Wilhelm Leibniz program, and the support of the TUM Institute for Advanced Study, funded by the German Excellence Initiative. This work was carried out with the support of the Karlsruhe Nano Micro Facility (KNMF [34]), a Helmholtz Research Infrastructure at Karlsruhe Institute of Technology (KIT). Florian Schaff thanks the TUM Graduate School for support. The authors thank C. Jud and S. Seyyedi for recording the wooden sticks data set. Finally, we thank the reviewers a lot for their very valuable suggestions.

*wieczore@cs.tum.edu

[1] A. Momose, S. Kawamoto, I. Koyama, Y. Hamaishi, K. Takai, and Y. Suzuki, Jpn. J. Appl. Phys. **42**, L866 (2003).
[2] T. Weitkamp, A. Diaz, C. David, F. Pfeiffer, M. Stampanoni, P. Cloetens, and E. Ziegler, Opt. Express **13**, 6296 (2005).
[3] F. Pfeiffer, M. Bech, O. Bunk, P. Kraft, E. F. Eikenberry, C. Brönnimann, C. Grünzweig, and C. David, Nat. Mater. **7**, 134 (2008).
[4] F. Pfeiffer, T. Weitkamp, O. Bunk, and C. David, Nat. Phys. **2**, 258 (2006).
[5] S. Schleede, M. Bech, K. Achterhold, G. Potdevin, M. Gifford, R. Loewen, C. Limborg, R. Ruth, and F. Pfeiffer, J. Synchrotron Radiat. **19**, 525 (2012).
[6] M. Stampanoni, Z. Wang, T. Thüring, C. David, E. Roessl, M. Trippel, R. A. Kubik-Huch, G. Singer, M. K. Hohl, and N. Hauser, Investigative Radiology **46**, 801 (2011).
[7] S. Schleede, F. G. Meinel, M. Bech, J. Herzen, K. Achterhold, G. Potdevin, A. Malecki, S. Adam-Neumair, S. F. Thieme, F. Bamberg, K. Nikolaou, A. Bohla, A. Ö. Yildirim, R. Loewen, M. Gifford, R. Ruth, O. Eickelberg, M. Reiser, and F. Pfeiffer, Proc. Natl. Acad. Sci. U.S.A. **109**, 17880 (2012).
[8] A. Yaroshenko, F. G. Meinel, M. Bech, A. Tapfer, A. Velroyen, S. Schleede, S. Auweter, A. Bohla, A. Ö. Yildirim, K. Nikolaou, F. Bamberg, O. Eickelberg, M. F. Reiser, and F. Pfeiffer, Radiology **269**, 427 (2013).
[9] A. Velroyen, M. Bech, A. Malecki, A. Tapfer, A. Yaroshenko, M. Ingrisch, C. C. Cyran, S. D. Auweter, K. Nikolaou, M. Reiser, and F. Pfeiffer, Phys. Med. Biol. **58**, N37 (2013).
[10] G. Potdevin, A. Malecki, T. Biernath, M. Bech, T. H. Jensen, R. Feidenhans'l, I. Zanette, T. Weitkamp, J. Kenntner, J. Mohr, P. Roschger, M. Kerschnitzki, W. Wagermaier, K. Klaushofer, P. Fratzl, and F. Pfeiffer, Phys. Med. Biol. **57**, 3451 (2012).
[11] F. Schaff, A. Malecki, G. Potdevin, E. Eggl, P. B. Noël, T. Baum, E. G. Garcia, J. S. Bauer, and F. Pfeiffer, Sci. Rep. **4**, 3695 (2014).
[12] V. Revol, B. Plank, R. Kaufmann, J. Kastner, C. Kottler, and A. Neels, NDT&E Int. **58**, 64 (2013).
[13] T. H. Jensen, M. Bech, I. Zanette, T. Weitkamp, C. David, H. Deyhle, S. Rutishauser, E. Reznikova, J. Mohr, R. Feidenhans'l, and F. Pfeiffer, Phys. Rev. B **82**, 214103 (2010).
[14] A. Malecki, G. Potdevin, T. Biernath, E. Eggl, E. G. Garcia, T. Baum, P. B. Noël, J. S. Bauer, and F. Pfeiffer, PLoS One **8**, e61268 (2013).
[15] A. Malecki, G. Potdevin, T. Biernath, E. Eggl, K. Willer, T. Lasser, J. Maisenbacher, J. Gibmeier, A. Wanner, and F. Pfeiffer, Europhys. Lett. **105**, 38002 (2014).
[16] J. Vogel, F. Schaff, A. Fehringer, C. Jud, M. Wieczorek, F. Pfeiffer, and T. Lasser, Opt. Express **23**, 15134 (2015).
[17] C. Jud, F. Schaff, I. Zanette, J. Wolf, A. Fehringer, and F. Pfeiffer, Dental materials **32**, 1189 (2016).
[18] $\mathbb{S}_2$ denotes the surface of the unit sphere, i.e., $\mathbb{S}_2 := \{u \in \mathbb{R}^2, \|u\| = 1\}$.
[19] M. Strobl, Sci. Rep. **4**, 7243 (2014).
[20] R. Andersson, L. F. v. Heijkamp, I. M. de Schepper, and W. G. Bouwman (IUCr Collaboration), J. Appl. Crystallogr. **41**, 868 (2008).
[21] In other words, $\int_{\mathbb{S}_2} 1 d\Omega(u) = 4\pi$.
[22] R. L. Siddon, Med. Phys. **12**, 252 (1985).
[23] P. M. Joseph, IEEE Trans. Med. Imaging **1**, 192 (1982).
[24] K. Hesse, I. H. Sloan, and R. S. Womersley, in *Handbook of Geomathematics* (Springer, Berlin, 2010), pp. 1185–1219.
[25] P. Delsarte, J. M. Goethals, and J. J. Seidel, Geometriae Dedicata **6**, 363 (1977).
[26] We denote the space of square integrable functions as $\mathcal{L}^2(\mathbb{S}_2) := \{f : \mathbb{S}_2 \to \mathbb{R}, \int f(u) d\Omega(u) < \infty\}$.
[27] K. Atkinson and W. Han, *Spherical Harmonics and Approximations on the Unit Sphere: An Introduction*, Lecture Notes in Mathematics Vol. 2044 (Springer, Berlin, 2012).
[28] T. Donath, M. Chabior, F. Pfeiffer, O. Bunk, E. Reznikova, J. Mohr, E. Hempel, S. Popescu, M. Hoheisel, M. Schuster, J. Baumann, and C. David, J. Appl. Phys. **106**, 054703 (2009).
[29] See Supplemental Material at http://link.aps.org/supplemental/10.1103/PhysRevLett.117.158101 for details of the setup and the measurements process.
[30] M. Wieczorek, J. Vogel, and T. Lasser, CampRecon Technical Report No. TUM-I1444, 2014.
[31] A. Fehringer, T. Lasser, I. Zanette, P. B. Noël, and F. Pfeiffer, in *SPIE Medical Imaging*, edited by S. Ourselin and M. A. Styner (SPIE, Bellingham, 2014), p. 90344F.
[32] A. Politis, Spherical harmonic transform library, https://github.com/polarch/Spherical-Harmonic-Transform.
[33] M. R. Hestenes and E. Stiefel, J. Res. Natl. Bur. Stand. **49**, 409 (1952).
[34] http://www.kit.edu/knmf.